RESEARCH ARTICLE | AUGUST 31 2023

Temperature dependent correlation of Hall effect and optical measurements of electron concentration in degenerate InN thin film

Fernando M. de Oliveira ; Chen Li ; Pijush K. Ghosh ; Andrian V. Kuchuk ; Morgan E. Ware ; Yuriy I. Mazur ; Gregory J. Salamo

Journal of Vacuum Science & Technology B 41, 052805 (2023)
https://doi.org/10.1116/6.0002866

JVST B
Journal of Vacuum Science & Technology B

ARTICLE

pubs.aip.org/avs/jvb

Temperature dependent correlation of Hall effect and optical measurements of electron concentration in degenerate InN thin film

Cite as: J. Vac. Sci. Technol. B 41, 052805 (2023); doi: 10.1116/6.0002866
Submitted: 2 June 2023 · Accepted: 14 August 2023 ·
Published Online: 31 August 2023

Fernando M. de Oliveira,[1,a)] Chen Li,[1] Pijush K. Ghosh,[1] Andrian V. Kuchuk,[1] Morgan E. Ware,[1,2] Yuriy I. Mazur,[1] and Gregory J. Salamo[1]

AFFILIATIONS

[1]Institute for Nanoscience and Engineering, University of Arkansas, Fayetteville, Arkansas 72701
[2]Department of Electrical Engineering, University of Arkansas, Fayetteville, Arkansas 72701

Note: This paper is part of the Special Topic Collection: Papers from the 48th Conference on the Physics and Chemistry of Surfaces and Interfaces (PCSI-48) 2023.

[a)]**Author to whom correspondence should be addressed:** fmaiade@uark.edu

ABSTRACT

In this work, we study the thermal evolution of the optical and electrical features of an InN thin film. By correlating photoluminescence (PL) and Hall effect results, we determine the appropriate values of the correlation parameter to be used in the empirical power law that associates the electron concentration with the linewidth of the PL spectrum, in the scope of the Burstein–Moss effect across a wide range of temperatures. Additionally, by associating Raman and PL results, we observe the thermally induced compressive strain widening of the bandgap of the InN film. Our findings demonstrate the reliability of optical methods in providing contactless measurements of electrical and structural features of semiconductors.

I. INTRODUCTION

Narrow bandgap semiconductors have become indispensable for advances in thermoelectronics and infrared systems.[1] In particular, indium nitride (InN) exhibits a direct bandgap of ~0.7 eV at room temperature, with a wide range of reported values in the literature, which when combined with its high electron mobility of $\sim 10^3$ cm^2/V s makes it exceptional for applications in high speed electronics, solar cells, and LEDs.[2] Its natural n-type character, resulting in general from the accumulation of electrons within a few nanometers of the surface, has allowed the successful use of InN nanosheets in 2DEG systems.[3] This charge accumulation is often attributed to the downward bands bending at the surface due to acceptor levels lying above the conduction band minimum.[4] The population of these localized states in the Gamma band (Γ) is determined by the band bending of approximately −0.2 and −0.4 eV at the $(000\bar{1})$ and (0001) surfaces, respectively.[5] The occupation of these states is influenced by the structural properties of the material, such as its morphology, interfaces, and level of strain, which can all be controlled during crystal growth.[6,7] Finally, external factors, such as pressure, applied fields, and temperature, play a role in controlling the effective population of these states and their subsequent transitions. In general, the evolution of a crystal band structure due to a thermal process will result in a shift of the Fermi energy level (E_F). In the case of InN, E_F is already situated in the conduction band due to the near-surface electron accumulation, and therefore, any increase in temperature will move E_F further into the conduction band.[3] As a consequence, a blueshift is observed in band-to-band transitions due to a band filling effect known as the Burstein–Moss shift, which has been demonstrated in many InN morphologies.[8] Photoluminescence (PL) measurements have allowed for the exploration of the charge density via the Burstein–Moss effect in a wide range of materials.[9] The correlation between the FWHM of the PL emission and the difference in energy between E_F and E_C, which is proportional to the number of occupied states, and therefore also to the electron concentration, n, can be described by an empirical power law.[10] The power law has

the simple form of Eq. (1),

$$FWHM \propto n^{\alpha}. \quad (1)$$

Here, α is a correlation parameter, which is determined empirically by comparison of PL spectra and Hall effect measurements at different temperatures.[11] In the case of InN, due to the surface charge accumulation, carriers in different subsurface depths may contribute differently to the Hall conductance. This must be considered in the interpretation of results derived from the Hall technique, especially for smaller structures.[12] Moreover, additional effects induced by low crystal quality and polymorphism also contribute to the luminescent *FWHM*, leading to errors in the determination of the correlation parameter. Values for α of ~0.50 have been reported for InN below 20 K, decreasing to 0.44 at 77 K and 0.39 at room temperature.[9,11,13] This temperature dependence of α and its importance to thin films, however, has not been systematically investigated. Therefore, in this work, we study the thermal evolution of the electron concentration in a thin InN film by semiempirically correlating electrical and optical results in order to determine the temperature behavior of the correlation parameter, α. At the same time, this will provide a useful tool to quickly determine the electron concentration in InN structures over a wide range of temperatures.

II. EXPERIMENT

A 300 nm thick InN film was grown by Molecular Beam Epitaxy (MBE) in a Veeco Gen-II plasma-assisted MBE system. The sample was grown on a GaN template made of ~5 μm of [0001]-oriented GaN grown on AlN/sapphire with a backside coating of titanium (~1 μm). Before the growth, the template was heat cleaned at 700 °C for 1 h in ultrahigh vacuum of $\sim 1 \times 10^{-10}$ Torr. An ~200 nm thick layer of Ga-polar undoped GaN was then grown as a buffer at 690 °C. The growth of the InN layer was performed at 400 °C. The nitrogen flow was set at 0.5 SCCM with a plasma power of 350 W, while the indium flux was set by the temperature of the In effusion cell, resulting in a beam equivalent pressure of $\sim 2.5 \times 10^{-7}$ Torr. High-resolution x-ray diffraction characterization was performed using a Philips X'pert MRD diffractometer equipped with standard four bounce Ge (220) monochromator on a 1.6 kW Cu Kα1 x-ray tube with vertical line focus and a three bounce (022) channel cut Ge analyzer crystal at the pixel detector.[14] Micro-PL characterizations were performed from 77 to 300 K. The PL signal was collected by a spectrometer (Horiba Jobin-Yvon, model LabRam HR800) equipped with an extended InGaAs single channel detector. The spot of the incident 632.8 nm He-Ne laser light (Melles Griot) was adjusted by the focus controllers of a microscope (Olympus BX41) using an objective lens with 100× magnification (Mitutoyo NIR100) resulting in an ~1 μm diameter excitation spot of ~5 mW. Micro-Raman characterizations were performed in this same system by using an electrically cooled Si CCD for signal collection. Hall characterizations were performed using the van der Pauw method from 10 to 300 K, applying a magnetic field of 5 kG perpendicular to the surface of the sample.

III. RESULTS AND DISCUSSION

The accumulation of electrons near the surface of the [0001]-oriented InN is illustrated in Fig. 1(a), which was generated by solving Poisson and Schrödinger equations for a 300 nm thick InN film using the software NEXTNANO.[15] See supplementary material for the InN parameters used in the simulation.

The transition between near-surface and bulk regions of the electron concentration in the InN structure can be roughly represented by the inflection point of the normalized charge profile found at the minimum of the derivative in Fig. 1(b) at ~7.8 nm. This value is within the range of values of 6–8 nm reported by Veal *et al.*[16] and Liu *et al.*[17] when interpreting Hall effect measurements of their InN

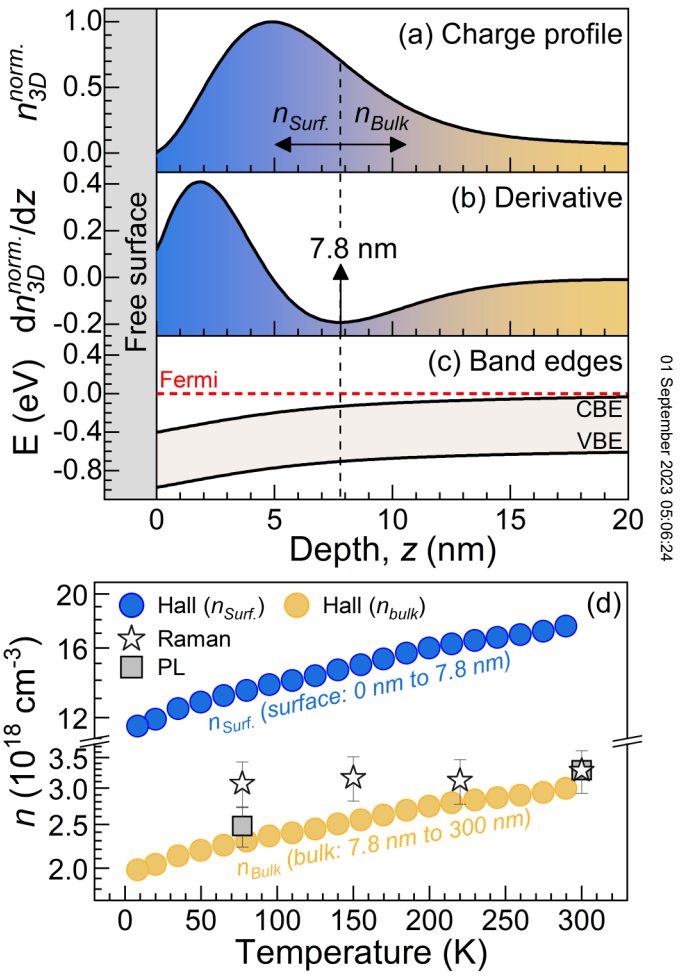

FIG. 1. Depth profile of the (a) electron concentration, (b) derivative of the charge distribution, and (c) conduction and valence band edges, CBE and VBE, respectively, near the free surface of the InN film. (d) Temperature dependence of the values of electron concentration determined using different methods: Hall effect assuming near-surface electron accumulation (blue circles in online version), Hall effect associated with the bulk region (yellow circles in online version), Raman results (stars), and PL results (squares).

films. For InN, the bending of the Γ band occurs along the depth delimited by the Thomas–Fermi screening length of InN, approximately within the first 10 nm in Fig. 1(c).[18] Some models have been proposed to describe the electronic conductivity considering the naturally nonuniform charge distribution in InN structures, such as a bilayer formed by an unintentionally doped near-surface layer with a low-conductivity volume underneath,[19] or a trilayer system, which additionally considers the interface between the InN film and its buffer or substrate as a separate path for conduction.[18] In both models, the effect of the charge accumulation on the parallel conductivity is reduced as the film becomes thicker. This is the result of the low mobility highly localized nature of the near-surface carriers.[18,20] Therefore, the interpretation of Hall conductance in terms of sheet carrier density and its conversion into volumetric electron concentration must take into account the effective depth where the probing is taking place, in order to avoid misestimation of the electronic population. For our 300 nm thick InN films, by considering the near-surface and bulk regions depicted in Fig. 1, the total electron concentration can be expressed by[16]

$$n_H^{2D}/(d_{Surf.}+d_{Bulk}) = n_H^{3D} = (n_{Surf.}^{3D} d_{Surf.} + n_{Bulk}^{3D} d_{Bulk})/(d_{Surf.}+d_{Bulk}). \quad (2)$$

Here, n_H^{2D} represents the sheet carrier density as measured directly by the Hall effect; $d_{Surf.} \approx 7.8$ nm is an approximation for the thickness of the region of near-surface charge accumulation determined from Fig. 1(b); $d_{Bulk} = 300 - d_{Surf.} \approx 292.2$ nm is the estimated thickness of the bulk region; n_H^{3D} is the volumetric electron concentration determined by the Hall effect measurements; while n_{Surf}^{3D} and n_{Bulk}^{3D} are the components of the volumetric electron concentration associated with the near-surface and bulk regions, respectively. Figure 1(a) allows the determination of the ratio $n_{Surf.}^{3D}/n_{Bulk}^{3D} \approx 5.8$ between the integrated electron concentration in the two regions.

The results derived from Hall effect measurements display a clear increase in electron concentration with temperature, as shown in Fig. 1(d), yielding values on the order of $\sim 10^{18}$ and $\sim 10^{19}$ cm^{-3} for the bulk and near-surface regions, respectively. In order to verify this trend by an alternative method, the InN film was studied by Raman spectroscopy. As an advantage, the Raman method of contactless determination of carrier density based on the plasmon-phonon coupled modes has been extensively investigated, and therefore it constitutes a reliable tool for the optical characterization of electronic properties.[7,21]

The insets of Figs. 2(a)–2(d) show the coupled mode, L^-, originating from the resonance between the electronic plasma and the longitudinal optical (LO) phonons of InN, with a wavevector oriented along the [0001] direction, identified as $A_1(LO)$.[21] The in-plane phonon mode $E_1(LO)$, defined along the (0001) plane, is forbidden in the backscattering geometry, and therefore it is not seen.[22] The frequency of L^-, seen for all the insets as a weak ~20 cm^{-1} wide band centered around ~425 cm^{-1}, can be described by the undamped solution of the dielectric function of the InN layer along its epitaxial axis,[23]

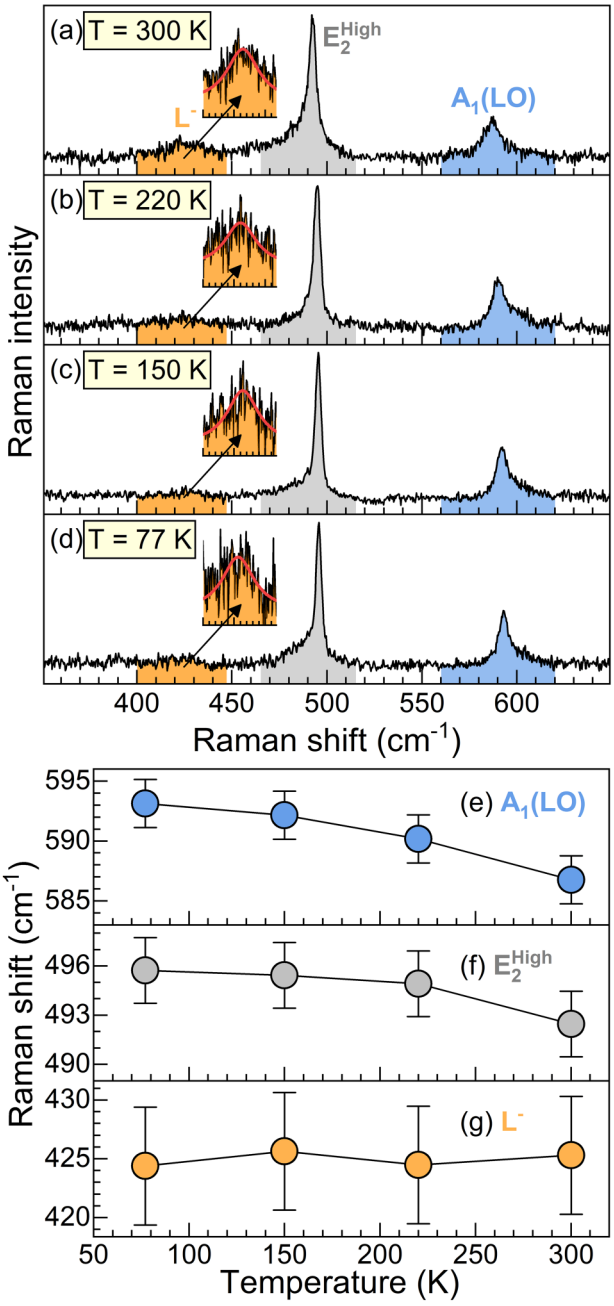

FIG. 2. Raman spectrum of the 300 nm thick InN film at (a) 300, (b) 220, (c) 150, and (d) 77 K. Thermal evolution of the frequency of the (e) A_1(LO), (f) E_2^{High}, and (g) L^- modes.

$$L^- = \left\{ (1/2)\left[(\omega_{LO})^2 + (\omega_P)^2 - \sqrt{[(\omega_{LO})^2 + (\omega_P)^2]^2 - 4(\omega_P)^2(\omega_{LO})^2 \varepsilon_\infty/\varepsilon_{st}} \right] \right\}^{1/2}, \quad (3)$$

where ω_{LO} and ω_P are phonon and plasmon frequencies, respectively, while $\varepsilon_\infty = 6.7$ and $\varepsilon_{st} = 9.5$ are the high frequency and static dielectric constants of InN, respectively.[21] Finally, by singling out ω_p in Eq. (3) and considering the electric field along the conductive layer as the driving force of the plasma motion, the number of electrons can be estimated in terms of the Drude theory by[21]

$$n_{Raman} = k\omega_p^2. \tag{4}$$

Here, k summarizes the constants: $k = m^*\varepsilon_0\varepsilon_\infty(2\pi c)^2/e^2 \cong 5.23 \times 10^{12}\,\mathrm{cm}^{-1}$, where $m^* = 0.07m_0$ is the electron effective mass; $\varepsilon_0 \cong 8.85 \times 10^{-12}\,\mathrm{Fm}^{-1}$ is the vacuum dielectric permittivity; $c = 299\,792\,498\,\mathrm{m\,s}^{-1}$ is the speed of light in vacuum, and $e \cong 1.602 \times 10^{-19}\,\mathrm{C}$ is the elementary charge.[21] Equation (4) yields the average value of $n_{Raman} \cong (3.2 \pm 0.2) \times 10^{18}\,\mathrm{cm}^{-3}$ along the entire range of temperatures. At room temperature, this value agrees very well with the results obtained via Hall effect measurements as scaled to the bulk region, seen in Fig. 1(d). For an incoming radiation of 632.8 nm, InN displays an absorption coefficient of $\sim 6.3 \times 10^4\,\mathrm{cm}^{-1}$, which represents a penetration depth of ~ 158 nm for the He-Ne laser into the InN film, therefore probing more than half of the bulk region.[24] By reducing the temperature of the InN film, its lattice is submitted to the additional influence of cooling-induced strain, which then dominates the behavior of the Raman modes. Raman scattering is extremely sensitive to the strained condition of the crystal, regardless of the temperature.[25] The nonpolar mode, E_2^{High}, is the most intense mode in Figs. 2(a)–2(d) representing the in-plane oscillations of the nitrogen atoms. It is found to shift to lower frequency as the temperature increases in Fig. 2(f).[26] A similar behavior is seen in Fig. 2(g) for the polar mode $A_1(LO)$. This shift to lower frequencies of both modes is the result of thermally induced changes in the lattice constant of the InN layer modifying the strain tensor of the crystal. Additionally, other contributions, such as anharmonic overtones and mismatch of thermal parameters at the buffer and substrate interfaces, have been theoretically reported to contribute to this frequency shift.[25] As a result, using the deformation potentials, $a = -610\,\mathrm{cm}^{-1}$ and $b = -857\,\mathrm{cm}^{-1}$, and the elastic constants, $C_{13} = 85$ GPa and $C_{33} = 236$ GPa, of InN associated with the evolution of the Raman modes, the lattice mismatch-induced strain can be determined by[26–28]

$$\epsilon_{\parallel} = \Delta\omega/[2a - (2C_{13}/C_{33})b] = -2\epsilon_{\perp}C_{13}/C_{33}. \tag{5}$$

Here, $\Delta\omega$ represents the difference between the measured frequency of the E_2^{High} mode and the frequency of the unstrained mode of InN, $\omega_0 = 488\,\mathrm{cm}^{-1}$. At 300 K, Eq. (5) results in the values of $\epsilon_{\parallel} \cong -7.4 \times 10^{-3}$ and $\epsilon_{\perp} \cong 5.3 \times 10^{-3}$, whereas at 77 K this increases to $\epsilon_{\parallel} \cong -1.3 \times 10^{-2}$ and $\epsilon_{\perp} \cong 9.2 \times 10^{-3}$, demonstrating the compression of the lattice with decreasing temperature similar to other reports of MBE grown InN layers.[25] The XRD technique was subsequently used to study the wurtzite crystal structure of the InN film, resulting in an almost fully relaxed crystal with residual strain of $\epsilon_{\parallel}^{XRD} \cong -4.2 \times 10^{-3}$ and $\epsilon_{\perp}^{XRD} \cong 3.0 \times 10^{-3}$, which is similar to that determined by Raman spectroscopy. See supplementary material for the XRD data.

In addition to a non-zero spontaneous polarization along $[000\bar{1}]$, the strained condition of the InN crystal manifests a piezoelectric effect that modifies its band structure, consequently influencing luminescence.[29] In our case, the small value of strain computed from Fig. 2 leads to an expected increase of a few meV in the bandgap due to compressive strain, which is within the range of uncertainty of the InN parameters according to the relation $\Delta E_g = K\epsilon_{\parallel}$, where $K = [(2c_c(C_{11} - C_{12})/C_{11}) + (2c_v(C_{11} - C_{12})/C_{11}) + (c_s(C_{11} + 2C_{12})/C_{11})]$, $c_c = -3.6$ eV, and $c_v = 0.92$ eV are the hydrostatic deformation potentials of the conduction and valence band edges, respectively, $c_s = -3.02$ eV is the shear deformation potential, and $C_{11} = 237$ GPa and $C_{12} = 106$ GPa are the elastic constants.[30–33] In the scope of Fermi statistics, the line shape of the PL spectrum can be described by the density of states projected onto a Fermi–Dirac distribution.[34] In particular, it has been shown that the high energy tail of the PL spectrum holds valuable information about the band-to-band transitions from degenerated carriers in semiconductors, while the low energy tail is associated with the Urbach energy at the absorption edge, which is also influenced by localized states within the bandgap.[34–36] In the absence of phonon-mediated indirect transitions, the line shape of the PL intensity for energies above the absorption band edge, E_G, at a temperature T can be approximately represented by $I(\hbar\omega) \propto (\hbar\omega - E_G)1/2\,\{1 + \exp[(\hbar\omega - E_G - E_F)/kT]\}$, where $\hbar\omega$ is the photon energy, E_F is the Fermi energy, and k is the Boltzmann constant.[34] In the case of InN, since its Fermi energy, E_F, is already above the conduction band minimum, the optical bandgap associated with band-to-band transitions is expected to produce luminescence around the energy represented by the difference $E_F - E_v$, where E_v represents the valence band edge. By raising the temperature, there is an increase in the number of occupied states at the conduction band. In this case, the Burstein–Moss shift of E_F into the conduction band increases the difference $E_F - E_C$, where E_C represents the conduction band edge.[10] As a consequence, a broadening limited by the lifetime of the occupied electronic levels is seen in the PL spectrum.[37] Therefore, since the number of occupied states at the conduction band edge is dependent on the difference $E_F - E_C$, by means of the Maxwell–Boltzmann approximation of the Fermi–Dirac function given by $n \approx N_C\exp[(E_F - E_C)/kT]$, where N_C represents the density of electrons in the conduction band, the linewidth of the PL spectrum can be used to determine carrier concentration, as seen in Eq. (1).[9,38]

In order to obtain the temperature dependence of the parameter α in Eq. (1), the PL spectrum of the InN film was acquired in a wide range of temperatures. As shown in Fig. 3(a), a thermally induced broadening of the PL spectrum was found. The full thermal evolution of the PL intensity depicted in Fig. 3(b) illustrates the broadening of the PL *FWHM*, which is represented by the area bounded by the green regions in this figure.

The emission energy associated with the optical bandgap of InN is shown in Fig. 3(b) by the white dashed line, E_{PL}, which is compared to the black dashed line that represents the Varshni relation, $E_g(T) = E_g(0) - \alpha_g T^2/(T + \beta_g)$, where E_g is the fundamental bandgap of InN, using parameters $\alpha_g = 0.41 \times 10^{-3}$ eV/K, $\beta_g = 454$ K, and $E_g(0) = 0.69$ eV, of bulk InN.[39] Clearly, the

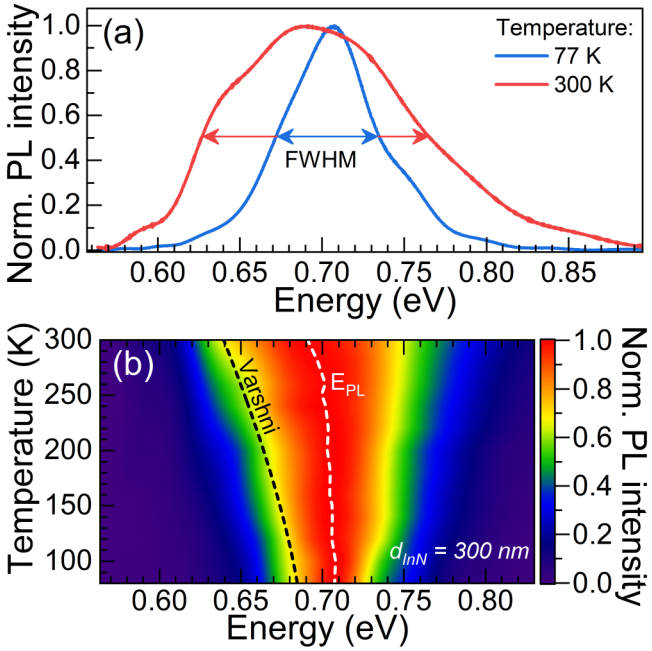

FIG. 3. (a) PL spectrum of the InN film at 77 and at 300 K. (b) Evolution of the PL intensity from 77 to 300 K. The white dashed line marks the emission center of the InN sample, while the black dashed line represents the expected shift for bulk InN.

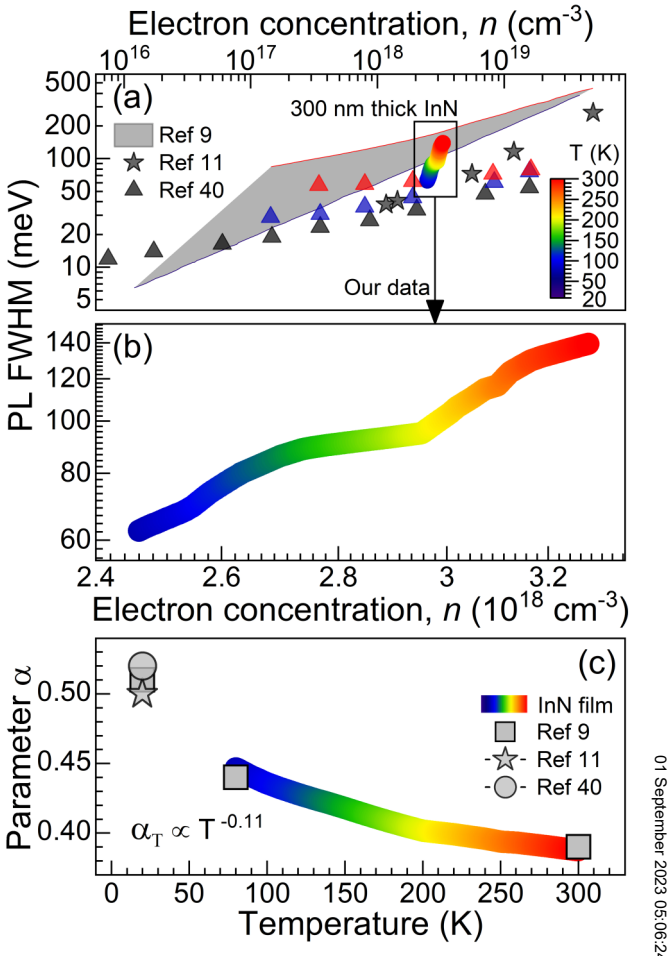

FIG. 4. (a) Values of *FWHM* from PL versus electron concentration of the InN film, compared with values from references. Note that the color (temperature) scale applies to all data points. (b) Zoomed range of the *FWHM* from PL versus electron concentration of the InN film. (c) Variation of the values of the parameter α along a wide range of temperatures of the InN film, compared with values from the literature. In the online version, the color (temperature) scale from black (20 K) to blue (77 K) to red (300 K) identifies the temperature of data acquisition in all plots here.

compressive strain in the InN films induced a widening of the bandgap by shifting $E_{PL}(T)$ to higher energies in Fig. 3(b) by a factor of $\Delta E \approx 25$ (55)meV at 77 (300)K. Using the values of strain obtained from the Raman spectra in Fig. 2, with the values of bandgap shift estimated from the PL results in Fig. 3, this energy shift represents an approximated value of $K = \Delta E_{PL}/\epsilon_{\parallel} \approx -1.9$ (−7.4)eV at 77 (300) K for the correlation constant. By using the values of the parameter α reported by Moret *et al.*[9] at 77 K ($\alpha = 0.44$) and at 300 K ($\alpha = 0.39$), the electron concentration determined by the PL method [see Eq. (1)] is very similar to the results obtained via Hall effect measurements scaled to the bulk concentration for both temperatures, as seen in Fig. 1(d). For instance, taking the logarithmic form of Eq. (1), the dependence between the PL linewidth and the electron concentration can be described by $\log(FWHM) = \alpha \log(n) + \beta$. Here, β is the residual of the correlation model. By fitting the electrical and optical results at the temperature of 300 K, we obtain $\alpha = 0.39$ with a residual of −5.2 in the logarithmic scale.

In order to now investigate the temperature dependence of the parameter α, the *FWHM* values of the PL spectra were correlated with the electron concentration determined via Hall effect measurements, as presented in Figs. 4(a) and 4(b), with the color bar representing the temperature. The bulk component of the electron concentration was employed to account for the considerable portion of the bulk volume of the InN sample that is penetrated by the excitation laser used in the PL experiment. Reference 9 was used to determine an acceptable range of values as shown by the gray area by modeling the free-electron recombination band transition of an ideal InN film.[9] This, along with other reports from the literature shown as data points in Fig. 4(a), shows that our results are well within the range of published values.[9,11,40] Additionally, it should be considered that the experimental data of Refs. 11 and 40 were acquired using PL measurements of InN films and nanowires, respectively.[11,40] Despite slightly different values of PL linewidth and electron concentration between these two references, likely due to morphology differences, both reported results follow the correlation model investigated in our study. Figure 4(b) illustrates in detail the behavior of the power law for our 300 nm InN film. Finally, the temperature dependence of the parameter α is presented in

Fig. 4(c). This was fit to the power law of Eq. (1), resulting in $\alpha(T) \approx 0.72 \times T^{-0.11}$. A similar trend is found by interpolating the reported results of Ref. 9, which gives $\alpha(T) \approx 0.62 \times T^{-0.08}$. Therefore, the correlation parameter α evolves from 0.39 to 0.44 by cooling the InN film from 300 to 77 K, finally reaching its reported value of ~0.51 at 10 K.

IV. CONCLUSIONS

In this study, by exploring Raman, PL, and Hall effect measurement results, we compared the thermal evolution of the optical and electrical features of a 300 nm thick InN film. Using these widely versatile measurements along with an understanding of the distribution of the electron density between the surface and the bulk states, we presented the temperature dependence (77–300 K) of the correlation parameter that governs the power law relation between the electron concentration and the PL FWHM. This is a result of the Burstein–Moss effect evolving across a wide range of temperatures. By comparing simulations with optical and electrical measurements, we found a difference of about 1 order of magnitude in the electron density between the near-surface and bulk regions of InN. Moreover, by using the results of both Raman and PL spectroscopic analyses, we demonstrated a correlation between the thermally induced compressive strain and the widening of the optical bandgap of the InN film. Our findings show the reliability of the optical methods in providing information through contactless measurements about electrical and structural features of InN films, which can be applied to other semiconductor materials as well.

ACKNOWLEDGMENT

This work was supported in part by the U.S. National Science Foundation Engineering Research Center for Power Optimization of Electro Thermal Systems (POETS) with Cooperative Agreement No. EEC-1449548.

AUTHOR DECLARATIONS

Conflict of Interest

The authors have no conflicts to disclose.

Author Contributions

Fernando M. de Oliveira: Data curation (equal); Formal analysis (equal); Visualization (equal); Writing – original draft (equal); Writing – review & editing (equal). **Chen Li:** Data curation (equal). **Pijush K. Ghosh:** Data curation (equal). **Andrian V. Kuchuk:** Conceptualization (equal); Writing – original draft (equal); Writing – review & editing (equal). **Morgan E. Ware:** Conceptualization (equal); Funding acquisition (equal); Writing – original draft (equal); Writing – review & editing (equal). **Yuriy I. Mazur:** Conceptualization (equal); Funding acquisition (equal); Writing – original draft (equal); Writing – review & editing (equal). **Gregory J. Salamo:** Funding acquisition (equal); Supervision (equal); Validation (equal).

DATA AVAILABILITY

The data that support the findings of this study are available from the corresponding author upon reasonable request.

REFERENCES

[1]X.-H. Li, Y.-X. Guo, Y. Ren, J.-J. Peng, J.-S. Liu, C. Wang, and H. Zhang, Front. Phys. **17**, 13304 (2022).
[2]T. D. Veal, C. F. McConville, and W. J. Schaff, *Indium Nitride and Related Alloys* (CRC, Boca Raton, FL, 2011).
[3]N. Syed *et al.*, ACS Nano **16**, 5476 (2022).
[4]C. G. Van de Walle and D. Segev, J. Appl. Phys. **101**, 081704 (2007).
[5]S.-C. Lin *et al.*, Appl. Phys. Express **5**, 031003 (2012).
[6]D. N. Lobanov, A. V. Novikov, B. A. Andreev, P. A. Bushuykin, P. A. Yunin, E. V. Skorohodov, and L. V. Krasilnikova, Semiconductors **50**, 261 (2016).
[7]F. M. Oliveira, A. V. Kuchuk, P. M. Lytvyn, C. Romanitan, H. V. Stanchu, M. D. Teodoro, M. E. Ware, Y. I. Mazur, and G. J. Salamo, ACS Appl. Nano Mater. **6**, 7582 (2023).
[8]K. S. A. Butcher, H. Hirshy, R. M. Perks, M. Wintrebert-Fouquet, and P. P.-T. Chen, Phys. Status Solidi A **203**, 66 (2006).
[9]M. Moret, S. Ruffenach, O. Briot, and B. Gil, Appl. Phys. Lett. **95**, 031910 (2009).
[10]R. M. Sieg and S. A. Ringel, J. Appl. Phys. **80**, 448 (1996).
[11]S. P. Fu, T. T. Chen, and Y. F. Chen, Semicond. Sci. Technol. **21**, 244 (2006).
[12]B. Arnaudov *et al.*, Phys. Rev. B **69**, 115216 (2004).
[13]P.-C. Wei *et al.*, Opt. Express **17**, 11690 (2009).
[14]H. V. Stanchu, A. V. Kuchuk, P. M. Lytvyn, Y. I. Mazur, M. E. Ware, Y. Maidaniuk, M. Benamara, Z. M. Wang, and G. J. Salamo, CrystEngComm **20**, 1499 (2018).
[15]S. Birner, T. Zibold, T. Andlauer, T. Kubis, M. Sabathil, A. Trellakis, and P. Vogl, IEEE Trans. Electron Devices **54**, 2137 (2007).
[16]T. D. Veal, L. F. J. Piper, W. J. Schaff, and C. F. McConville, J. Cryst. Growth **288**, 268 (2006).
[17]W. Liu, R. J. N. Tan, C. B. Soh, and S. J. Chua, Appl. Phys. Lett. **97**, 042110 (2010).
[18]P. D. C. King, T. D. Veal, and C. F. McConville, J. Phys.: Condens. Matter **21**, 174201 (2009).
[19]A. Mekys, J. Jurkevičius, A. Kadys, M. Kolenda, V. Kovalevskij, and G. Tamulaitis, Thin Solid Films **692**, 137619 (2019).
[20]L. Hsu, R. E. Jones, S. X. Li, K. M. Yu, and W. Walukiewicz, J. Appl. Phys. **102**, 073705 (2007).
[21]J. S. Thakur, D. Haddad, V. M. Naik, R. Naik, G. W. Auner, H. Lu, and W. J. Schaff, Phys. Rev. B **71**, 115203 (2005).
[22]E. O. Schäfer-Nolte, T. Stoica, T. Gotschke, F. A. Limbach, E. Sutter, P. Sutter, D. Grützmacher, and R. Calarco, Nanotechnology **21**, 315702 (2010).
[23]S. Lazić, E. Gallardo, J. M. Calleja, F. Agulló-Rueda, J. Grandal, M. A. Sánchez-Garcia, E. Calleja, E. Luna, and A. Trampert, Phys. Rev. B **76**, 205319 (2007).
[24]J. Wu, W. Walukiewicz, K. M. Yu, J. W. Ager III, E. E. Haller, H. Lu, W. J. Schaff, Y. Saito, and Y. Nanishi, Appl. Phys. Lett. **80**, 3967 (2002).
[25]X. D. Pu, J. Chen, W. Z. Shen, H. Ogawa, and Q. X. Guo, J. Appl. Phys. **98**, 033527 (2005).
[26]A. V. Kuchuk, F. M. de Oliveira, P. K. Ghosh, Y. I. Mazur, H. V. Stanchu, M. D. Teodoro, M. E. Ware, and G. J. Salamo, Nano Res. **15**, 2405 (2021).
[27]F. M. Morales, J. M. Mánuel, R. García, B. Reuters, H. Kalisch, and A. Vescan, J. Phys. D: Appl. Phys. **46**, 245502 (2013).
[28]V. Cimalla *et al.*, Phys. Status Solidi C **0**, 2818 (2003).
[29]C. X. Ren, Mater. Sci. Technol. **32**, 418 (2016).
[30]S. X. Li, J. Wu, E. E. Haller, W. Walukiewicz, W. Shan, H. Lu, and W. J. Schaff, Appl. Phys. Lett. **83**, 4963 (2003).
[31]Q. Yan, P. Rinke, M. Scheffler, and C. G. Van de Walle, Appl. Phys. Lett. **97**, 181102 (2010).

[32]M. K. Mahata, S. Ghosh, S. K. Jana, A. Chakraborty, A. Bag, P. Mukhopadhyay, R. Kumar, and D. Biswas, AIP Adv. **4**, 117120 (2014).
[33]G. Gonzalez De La Cruz, A. Calderon Arenas, and H. Herrera, J. Appl. Phys. **98**, 023501 (2005).
[34]V. Y. Davydov *et al.*, Phys. Status Solidi B **230**, R4 (2002).
[35]E. Ugur, M. Ledinský, T. G. Allen, J. Holovský, A. Vlk, and S. De Wolf, J. Phys. Chem. Lett. **13**, 7702 (2022).
[36]E. Baron, R. Goldhahn, M. Deppe, D. J. As, and M. Feneberg, Phys. Status Solidi B **257**, 1900522 (2020).
[37]O. Svelto and D. C. Hanna, *Principles of Lasers (Vol. 1)* (Springer, New York, 2010).
[38]L. A. Coldren, S. W. Corzine, and M. L. Mašanović, "Appendix two: Relationships between Fermi energy and carrier density and leakage," in *Diode Lasers and Photonic Integrated Circuits* (Wiley., New York, 2012), pp. 529–544.
[39]I. Vurgaftman and J. R. Meyer, J. Appl. Phys. **94**, 3675 (2003).
[40]Y.-L. Chang, Z. Mi, and F. Li, Adv. Funct. Mater. **20**, 4146 (2010).